Journal of Power Sources 232 (2013) 66–73

Contents lists available at SciVerse ScienceDirect

Journal of Power Sources

journal homepage: www.elsevier.com/locate/jpowsour

Sputtered nanocrystalline coating of a low-Cr alloy for solid oxide fuel cell interconnects application

Shujiang Geng [a,b,*], Yaohua Li [a], Zhonghe Ma [a], Shenglong Zhu [b], Fuhui Wang [b]

[a] School of Materials and Metallurgy, Box 119, Northeastern University, 3-11 Wenhua Road, Shenyang 110819, China
[b] State Key Laboratory for Corrosion and Protection, Institute of Metal Research, Chinese Academy of Sciences, 62 Wencui Road, Shenyang 110016, China

HIGHLIGHTS

- Sputtered coating of a low-Cr Fe–Co–Ni alloy with 0.36wt.% Si was prepared.
- Oxidation resistance of the sputtered coating was extremely improved in air at 800 °C.
- The surface scale structure with a low-Cr containing $(Fe,Co)_3O_4$ spinel atop Cr_2O_3 formed on the sputtered coating.
- The spinel layer served as an effective barrier to Cr outward migration.
- The surface scale exhibited a good electrical conductivity.

ARTICLE INFO

Article history:
Received 12 November 2012
Received in revised form
8 January 2013
Accepted 10 January 2013
Available online 21 January 2013

Keywords:
Low-chromium alloy
Sputtered coating
Oxidation
Area specific resistance

ABSTRACT

Sputtered coating of a low-Cr Fe–Co–Ni alloy with 0.36wt.% Si has been prepared on the same cast alloy via magnetron sputtering method. The sputtered low-Cr alloy coating with columnar nanocrystalline structure is thermally oxidized in air at 800 °C corresponding to the cathode atmosphere of solid oxide fuel cell (SOFC). It is found that the oxidation resistance of the sputtered low-Cr alloy coating is significantly improved in comparison with the cast low-Cr alloy. A double-layer oxide scale is thermally developed on the sputtered low-Cr alloy coating after oxidation for 12 weeks. The outer layer is $(Co,Fe)_3O_4$ spinel containing small amount of Ni and Cr. The inner layer is a continuous Cr_2O_3 layer, followed by oxides of $CrNbO_4$ and Nb_2O_5. The surface scale formed on the sputtered coating after 12-week thermal exposure demonstrates an area specific resistance (ASR) of 31.97 mΩ cm^2. The sputtered low-Cr alloy nanocrystaline coating exhibits a promising perspective for intermediate temperature SOFC interconnects application.

1. Introduction

Recently, significant progress has been obtained by reducing thickness of the electrolyte [1,2] or by using novel electrolytes with high oxygen-ion conductivity [3–5] in order to operate a solid oxide fuel cell (SOFC) at intermediate temperatures (600–800 °C). Such progress has made it possible to employ metal alloys as interconnects. Metal alloys are preferable to the traditional $LaCrO_3$-based ceramic interconnect materials [6–8], since they are much cheaper and more formable, allowing for the fabrication of more complex-shaped interconnects.

The metal alloys being explored for interconnect applications included Cr-based [9], Ni-based [10–12] and Fe-based [13–15] alloys. All of them are Cr_2O_3-forming alloys due to the relatively high electrical conductivity of Cr_2O_3, as compared to Al_2O_3 and SiO_2 [7,16]. Nonetheless, the Cr_2O_3-forming alloys have an inherent weakness, i.e. the formation of volatile Cr(VI) species under operating environments of SOFC cathode owing to the Cr_2O_3 evaporation. The volatile Cr(VI) species may migrate to and thus poison the cathode [17], leading to the deterioration of cell performance [18–20]. For metal alloys interconnects, therefore, the formation of a stable, electrically conductive and low-Cr volatility oxide outer layer atop the Cr_2O_3 is highly desirable to resolve the Cr-poisoning issue. Indeed, a novel low-Cr Fe–Co–Ni base alloy has been recently developed for SOFC interconnect applications, which upon thermal exposure forms a double-layer oxide structure with $(Fe,Co,Ni)_3O_4$ spinel as the outer layer and Cr_2O_3 as the inner layer in contact with internal oxides including Si individual oxide

* Corresponding author. School of Materials and Metallurgy, Box 119, Northeastern University, 3-11 Wenhua Road, Shenyang 110819, China. Tel.: +86 24 83673860; fax: +86 24 83687731.
E-mail addresses: gengsj@smm.neu.edu.cn, gengshujiang@yahoo.com (S. Geng).

0378-7753/$ – see front matter © 2013 Elsevier B.V. All rights reserved.
http://dx.doi.org/10.1016/j.jpowsour.2013.01.067

particles [21]. The double-layer oxide structure demonstrated an excellent oxidation resistance and electrical conductivity. Importantly, the spinel outer layer significantly blocked the Cr volatility from the inner layer of Cr_2O_3. However, Si with content of 1.5wt.% at least must be added into the low-Cr alloy in order to promote the formation of a continuous Cr_2O_3 inner layer. Hence, the potential challenge for this alloy is that the discrete internal oxide particles of SiO_2 underneath Cr_2O_3 layer might become a continuous layer which has a quite high electrical resistivity, subsequently resulting in stack malfunction.

In order to avoid the formation of a continuous SiO_2 layer, a similar low-Cr alloy with 0.36 wt.%Si which is an acceptable level for SOFC interconnect applications have been made. A columnar nanocrystalline coating was deposited on the cast low-Cr alloy with identical composition by means of magnetron sputtering method. The short-term oxidation behavior of the sputtered low-Cr alloy coating indicated that a double-layer oxide structure with an outer layer consisted mainly of $(Co,Fe)_3O_4$ spinel atop an inner layer of Cr_2O_3 was thermally grown [22], even though the content of Si was much lower than 1.5wt.%. In this paper, details regarding long-term oxidation behavior and surface scale electrical conductivity of the sputtered low-Cr alloy nanocrystalline coating are evaluated and discussed in air at 800 °C corresponding to the SOFC cathode environment.

2. Experimental

A low-Cr Fe–Co–Ni base alloy with chemical composition (in weight percent) of 30.3% Co, 24.03% Ni, 5.71% Cr, 4.62% Nb, 0.36% Si, 0.053% Y, <0.05% Mn, 0.0023% P, 0.0034% C, <0.001% S, and the balance Fe, was prepared in a vacuum-induction furnace. The samples (15 × 10 × 1.5 mm) used as the substrate for coating deposition were cut from an ingot by an electric-discharge machining (EDM). After drilling a hole with a diameter of 1.5 mm in the upper center of the sample, each sample was ground to 600-grit with silicon carbide papers. Then they were sandblasted, followed by ultrasonic cleaning in acetone before sputtering. The target was the identical cast low-Cr alloy sheet of 248 × 124 mm^2. The sputtering deposition was conducted for 24 h with argon pressure of 0.12 Pa, substrate heating temperature of 180 °C and the sputtering target DC power of 1.2 kW. The substrate samples for coating were rotating in front of the target during sputtering so that all sides of the sample were deposited uniformly.

The thermal expansion behavior of the low-Cr Fe–Co–Ni alloy with 0.36wt.% Si was measured using a dilatometer with rectangle bar (length, 8 mm; width, 1 mm; height, 1 mm). The thermal expansion measurement was conducted from 50 to 800 °C in air.

Oxidation testing of both the cast alloy and its sputtered nanocrystalline coating was conducted in a box furnace. The samples were hung in alumina crucibles. The cast alloys were oxidized in air at 800 °C for total 6 weeks, and the sputtered coatings were oxidized for total 12 weeks. The weight of each sample was measured after furnace cooling to room temperature following each 1-week thermal exposure.

The surface and cross-section morphologies of the samples were observed by scanning electron microscopy (SEM) with an energy dispersive X-ray spectroscopy (EDX). The sputtered coating was examined using transmission electron microscopy (TEM) to determine the size of the columnar grain. The phase structures of the samples were identified with X-ray diffraction (XRD).

Electrical resistance of oxidized samples was measured between 600 and 800 °C in air using 4-point method. The measurement setup was described in our previous work [23]. Two of the oxidized surfaces were covered with Pt paste, followed by curing at 800 °C in air for 1 h. Each Pt foil had two welded Pt leads. Two alumina rods and springs were used to apply pressure and clamp the assembly together during measurement. A constant current of 10 mA (I) was applied across two Pt leads by a current source, and then the corresponding voltage (V) across the other two leads was measured by a multimeter. The resistance (R) was calculated according to the Ohm's law, $R = V/2I$. A factor of 2 was included to account for the measured voltage across two oxide scales. The area specific resistance (ASR) of the oxide scale was then equal to R multiplied by the area covered by the Pt paste.

3. Results and discussion

3.1. Thermal expansion behavior of the low-Cr alloy

Fig. 1 shows the thermal expansion behavior of this low-Cr alloy with 0.36wt.% Si. It exhibited a good match in thermal expansion behavior with other cell components, including the electrolyte, cathode and anode in the temperature range of 200–800 °C, similar to that of the low-Cr alloy with 1.5wt.% Si [21], indicating that the decrease of Si content from 1.5wt.% to 0.36wt.% did not obviously influence the thermal expansion behavior of the low-Cr alloy.

3.2. Characterization of the sputtered coating

The SEM surface morphology of the sputtered low-Cr alloy coating is shown in Fig. 2. The surface appearance of the sputtered coating looks like cauliflowers with columnar grain structure, and the diameter of the columnar grain is lower than 10 nm, as demonstrated in the inserted images including the SEM fractured cross-section and TEM bright field micrograph. It was concluded that the low-Cr alloy sputtered coating was composed of the columnar nano-grains. Moreover, the phase structure of the sputtered coating is the same as its cast alloy [22]. Clearly, a large number of interfaces were observable between different cauliflowers, which were also present between columnar grains from the SEM cross-section view. It was the interfaces or grain boundaries that significantly changed the oxidation behavior of the sputtered coating upon thermal exposure in the environment of SOFC cathode as discussed later.

3.3. Oxidation behavior

3.3.1. Oxidation kinetics

Fig. 3 depicts the mass gain of the sputtered low-Cr alloy nanocrystalline coating as a function of oxidation time in air at

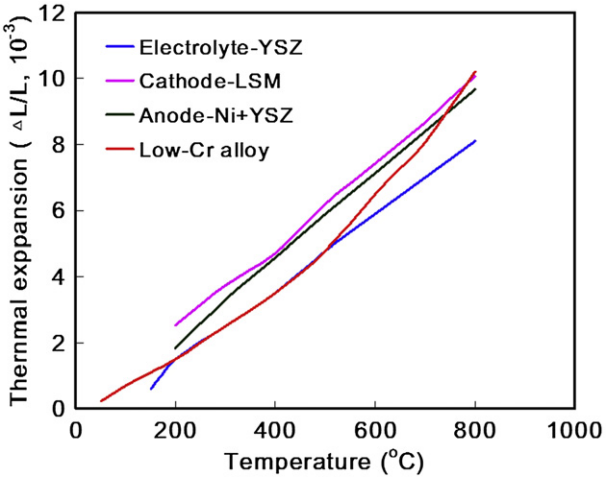

Fig. 1. Thermal expansion vs. temperature for the low-Cr alloy with 0.36wt.% Si, as compared to other cell components.

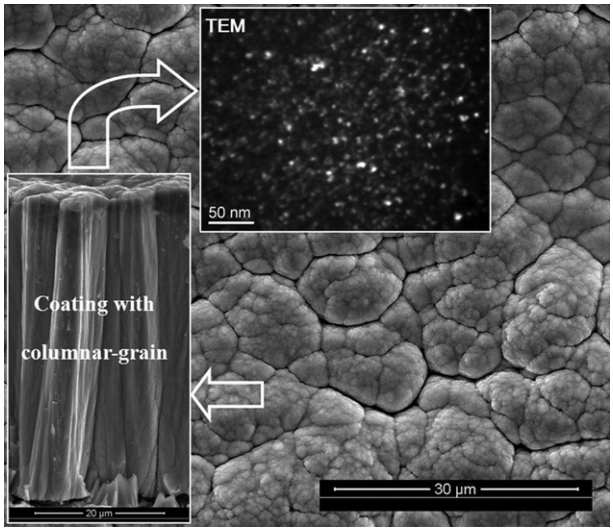

Fig. 2. SEM morphologies and TEM micrograph of the sputtered low-Cr alloy coating.

800 °C, in comparison with its cast alloy. For the cast alloy, apparently, the mass gain increased sharply before the 3rd week, and then still elevated with oxidation time. In contrast to the cast alloy, the sputtered nanocrystalline coating experienced a rapid mass gain during the 1st week thermal exposure, followed by a slight increase over the oxidation time. It was found in Fig. 4 that the oxidation kinetics of the sputtered coating from the 1st week to the 12th week almost obeyed a parabolic law:

$$\left(\frac{\Delta W}{A}\right)^2 = K_P t \quad (1)$$

where $\Delta W/A$ is the mass gain per unit area at oxidation time, t, while K_P is the parabolic rate constant equal to the slope of the fitting line originated from the actually measured points shown in Fig. 4. After oxidation for 40,000 h (lifetime expected for SOFC stacks) that is equal to 238.1 weeks, the mass gain of the sputtered coating was calculated according to the fitting line equation:

$$y = 0.23x + 1.54 \quad (2)$$

The calculated result of the mass gain per unit area was 7.5 mg cm^{-2} which was slightly lower than that of the cast alloy after 1-week oxidation, and was much lower than that of the cast alloy after 6-week oxidation under the same oxidizing condition, as indicated in Figs. 3 and 5 of the predicted oxidation kinetics for the sputtered coating, implying a protective oxide layer should be developed on it.

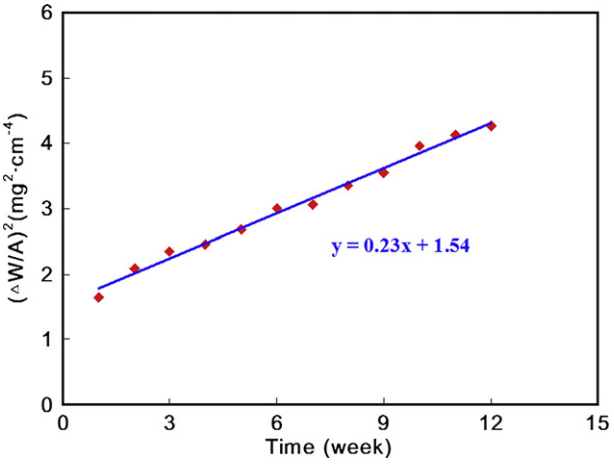

Fig. 4. Parabolic oxidation kinetics of the sputtered low-Cr alloy coating in air at 800 °C.

3.3.2. Morphologies, compositions and structures of the surface oxides

SEM surface scale morphologies and compositions of the cast low-Cr alloy after 6-week thermal exposure in air at 800 °C are shown in Fig. 6. Spalling of the surface scale was clearly observable as demonstrated in Fig. 6a. The surface appearances were obviously different between non-spalling area 1 and spalling area 2, as shown in Fig. 6b and c of the SEM expanded images from area 1 and area 2 in Fig. 6a, respectively. From Fig. 6d and e of EDX spectra, however, their compositions were similar and composed of Co and Fe oxides. Fig. 7 shows the surface oxide scale morphologies of the sputtered coating after oxidation for 12 weeks under the identical condition of thermal exposure. The surface was quite different from that of the cast alloy after oxidation, and was free of spallation as shown in Fig. 7a of the SEM image with lower magnitude. Notably, there were some interfaces on the scale surface, as indicated in Fig. 7b of the SEM image with higher magnitude, which might be resulted from the original interfaces between different cauliflowers or columnar grains (Fig. 2). The EDX spectra presented in Fig. 7c that the surface scale formed on the sputtered nanocrystalline coating contained oxides of Cr, Fe, Co, Ni and Nb. In comparison with the cast alloy, it

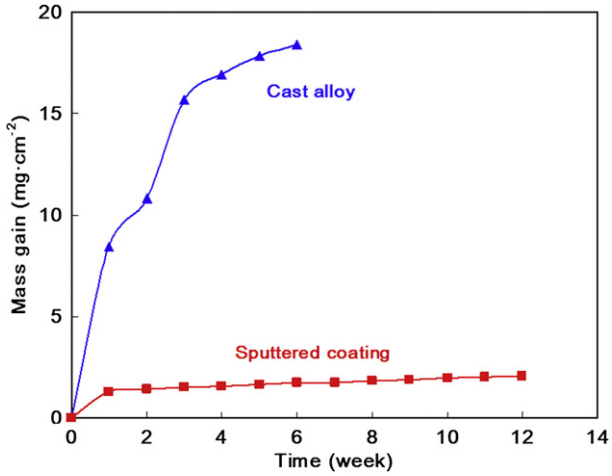

Fig. 3. Oxidation kinetics of the cast low-Cr alloy and its sputtered coating in air at 800 °C.

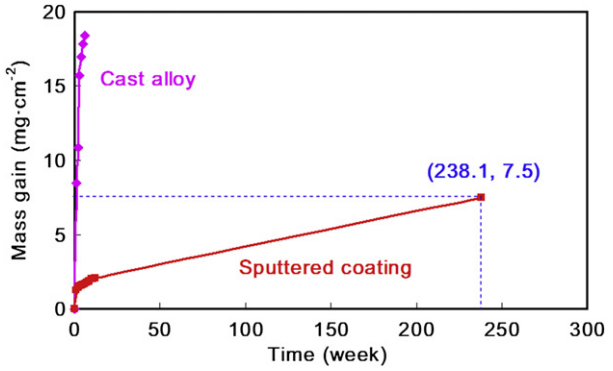

Fig. 5. Predicted oxidation kinetics of the sputtered low-Cr alloy coating in air at 800 °C.

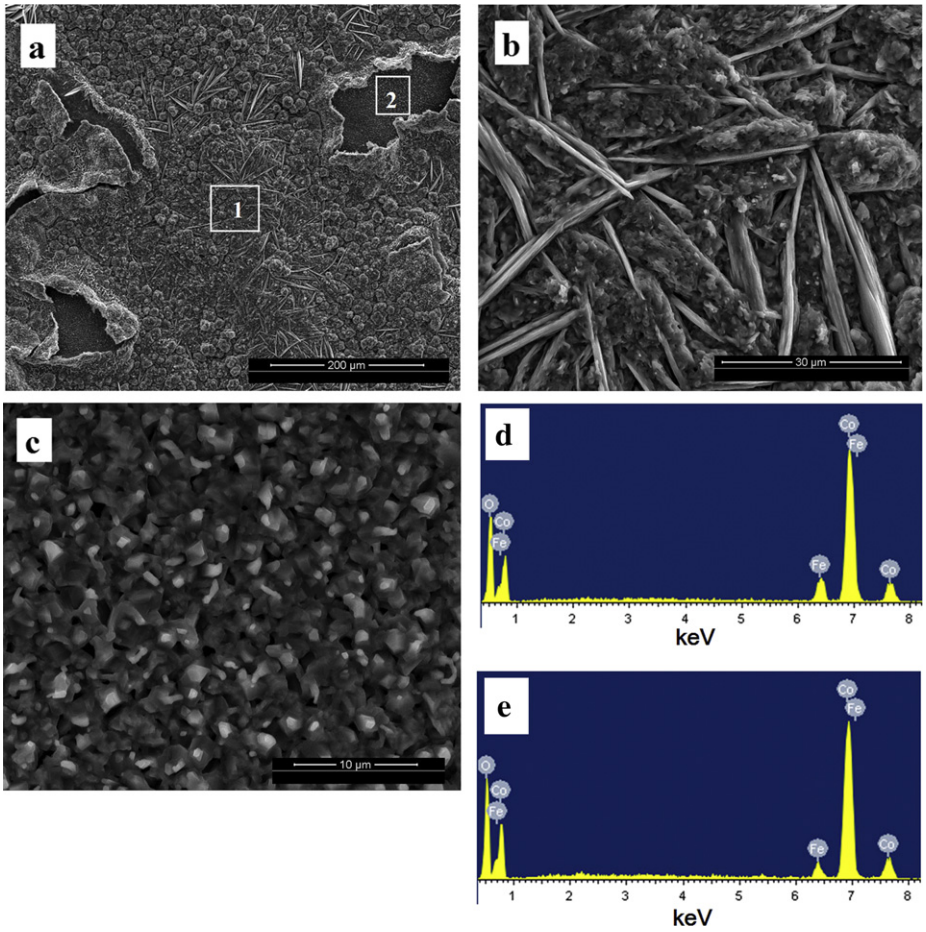

Fig. 6. Surface morphologies and EDX analyses of the cast low-Cr alloy after oxidation for 6 weeks in air at 800 °C, (a) surface SEM image; (b) expanded view from area 1; (c) expanded view from area 2; (d) EDX spectra from area 1; (e) EDX spectra from area 2.

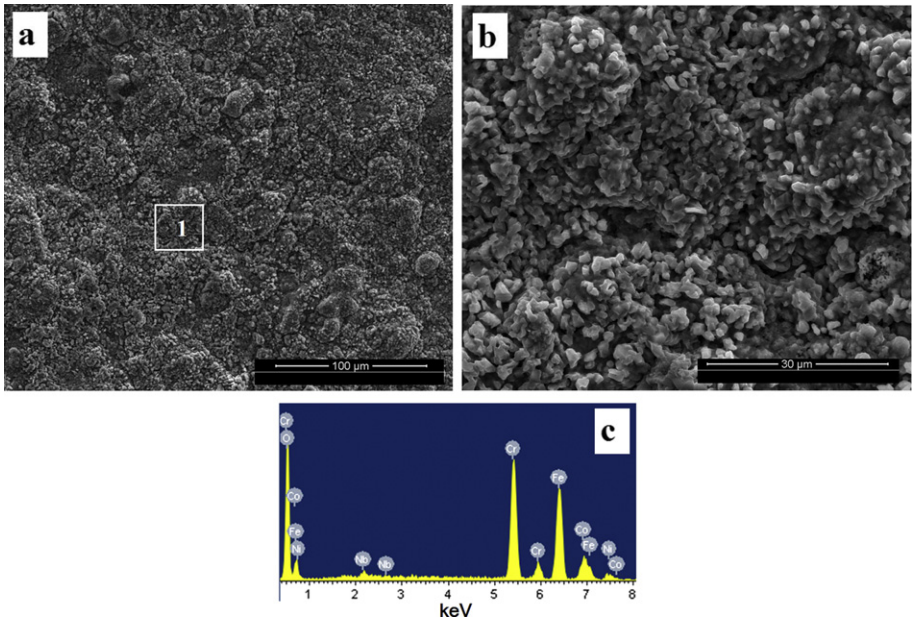

Fig. 7. Surface morphologies of the low-Cr alloy sputtered coating after oxidation for 12 weeks in air at 800 °C, (a) surface SEM image; (b) expanded view from area 1; (c) EDX spectra from area 1.

can be seen that the sputtered coating of the low-Cr alloy has completely changed the surface scale morphology and composition.

SEM cross-sectional views with lower magnitude of the oxidized samples are shown in Fig. 8. The oxide scale thermally formed on the cast low-Cr alloy after 6-week oxidation in air at 800 °C contained external and internal oxides (Fig. 8a). The external oxides layer was thick, which led to the formation of pores and cracks at the interface between external oxides layer and internal oxidation zone, and subsequent the detachment of the surface oxide as shown in Fig. 6a. Nevertheless, the oxide scale developed on the sputtered low-Cr alloy coating after 12-week oxidation exhibited a complete adherence to the surface (Fig. 8b). It was a uniform oxide scale much thinner than that on the cast alloy after 6-week oxidation. Fig. 9 presents SEM cross-sections with elements line scan of the cast alloy after thermal exposure in air at 800 °C. After 1-week oxidation, the surface oxide scale that was around 100 μm thick contained external oxides layer (around 55 μm thick) and internal oxidation zone (around 45 μm thick) as shown in Fig. 9a. The external oxides layer was Co-rich oxide in the outmost surface, followed by Co/Fe-rich oxide containing small amount of Ni near the internal oxidation zone. The internal oxidation zone was comprised mainly of Cr oxide. It was found that the surface oxide scale became thick with increasing oxidation time, consistent with the oxidation kinetics (Fig. 3). As shown in Fig. 9b, the scale with a thickness about 230 μm was formed on the cast low-Cr alloy after 6-week oxidation. It was also composed of the external oxides layer (about 130 μm) and internal oxidation zone (about 100 μm). The distribution of the surface oxides formed on the cast alloy after 6-week oxidation was similar to that after 1-week oxidation. However, a uniform and thin oxide scale was developed on the sputtered nanocrystalline coating after 12-week oxidation, as indicated in Fig. 8b. The cross-section details of the scale are shown in Fig. 10a. The thickness of the scale was around 25 μm much thinner than that on the cast alloy after thermal exposure only for 1 week. It thermally formed a double-layer oxide structure with an outer layer rich in Fe and Co containing small amount of Ni and Cr atop an inner layer rich in Cr, in contact with Nb/Cr-rich oxides with small amount of Si, as shown in Fig. 10b that presents the EDX spectra from point 1 in Fig. 10a. In case of the outer layer, in detail, it was rich in Fe and Co with small amount of Ni and Cr near the outer surface, while it was rich in Fe with small amount of Co and Cr near the Cr-rich inner layer, as indicated from the elements line scan (Fig. 10a). Evidently, it was the formation of the continuous Cr-rich oxide inner layer that significantly improved the oxidation resistance of the sputtered coating, consistent with the oxidation kinetics shown in Fig. 3.

Fig. 11 presents X-ray diffraction patterns of the samples after oxidation in air at 800 °C. Combined with elements line scan analyses above, the oxide scale formed on the low-Cr cast alloy after 1-week oxidation contained Co_3O_4 and $(Co,Fe)_3O_4$, i.e. the external oxides layer consisted mainly of the $(Co,Fe)_3O_4$ spinel phase underneath the outmost surface of Co_3O_4 phase. The XRD patterns did not show the diffraction peaks of the internal oxides due to the thick external oxides layer that blocked the X-ray penetration. According to the SEM cross-sections and elements line scan analyses (Fig. 9b) of the oxide scale formed on the cast alloy, the distribution of surface oxides grown on it after 6-week oxidation was similar to that after 1-week oxidation. In contrast to the cast alloy, from the XRD patterns (Fig. 11) combined with elements line scan and EDX point analyses (Fig. 10), the surface oxide scale thermally developed on the sputtered coating primarily contained Cr_2O_3, $(Co,Fe)_3O_4$, $CrNbO_4$ and Nb_2O_5. Thus the oxide scale was comprised of the outer $(Co,Fe)_3O_4$ spinel layer incorporated with small amount of Ni and Cr, underneath which the inner layer of Cr_2O_3 was formed, followed by some oxides including $CrNbO_4$ and Nb_2O_5 with small amount of Si. The Si-containing oxide could not be present in XRD patterns most likely due to the fact that its content was not high enough to be detected or its phase structure was amorphous. The Si oxide should be discontinuous, which is consistent with ASR results shown later.

From Figs 9–11, it is evident that the surface oxide scale formed on the cast alloy is completely different from that on its sputtered nanocrystalline coating. For the cast low-Cr alloy, an external oxides layer with the structure of an outer surface layer of Co_3O_4 atop a spinel layer of $(Co,Fe)_3O_4$ containing small amount of Ni in contact with an internal oxidation zone consisted mainly of Cr oxide was formed upon thermal exposure. The spinel layer contained only minor Ni and almost no Cr was detected probably due to their lower outward diffusion rates in comparison with Fe and Co. The Cr internal oxide could not become continuous layer, since the Si content in the alloy was not high enough to promote the formation of a continuous Cr_2O_3 inner layer [21]. On the contrary, a double-layer oxide structure with an outer layer of $(Co,Fe)_3O_4$ spinel containing small amount of Ni and Cr, followed by an inner layer of Cr_2O_3 in contact with $CrNbO_4$ and Nb_2O_5 was thermally grown on the sputtered nanocrystalline coating. In the initial stage of thermal exposure, nuclei of all the stable oxides including Fe, Co, Ni and Cr formed on the sputtered coating surface owing to the nanocrystallization that promoted their oxidation rates [24]. This led to a rapid mass gain as shown in Fig. 3, and subsequent formation of the $(Co,Fe)_3O_4$ spinel layer containing small amount of Ni and Cr as indicated in Figs. 10 and 11. After the formation of the spinel layer rich in Fe and Co, Cr was enriched near the coating substrate adjacent to the oxide scale because of the depletion of Fe and Co. Furthermore, the oxygen partial pressure at the spinel/coating interface became low due to establishment of the surface spinel

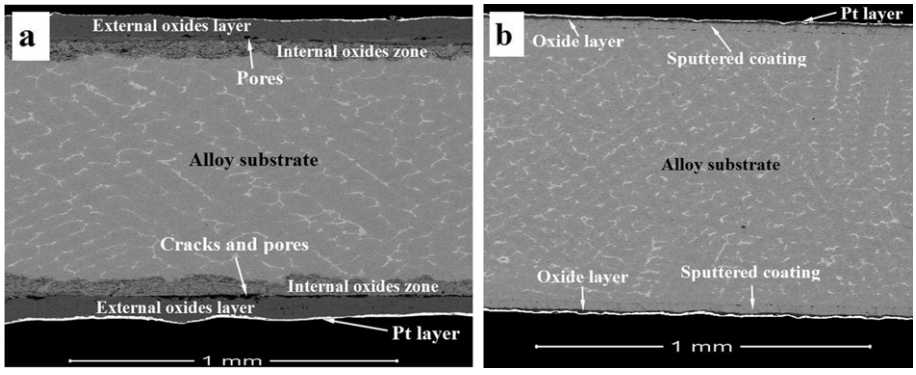

Fig. 8. Low magnitude cross-section images of the cast low-Cr alloy (a) and its sputtered coating (b) after oxidation in air at 800 °C for 6 and 12 weeks, respectively.

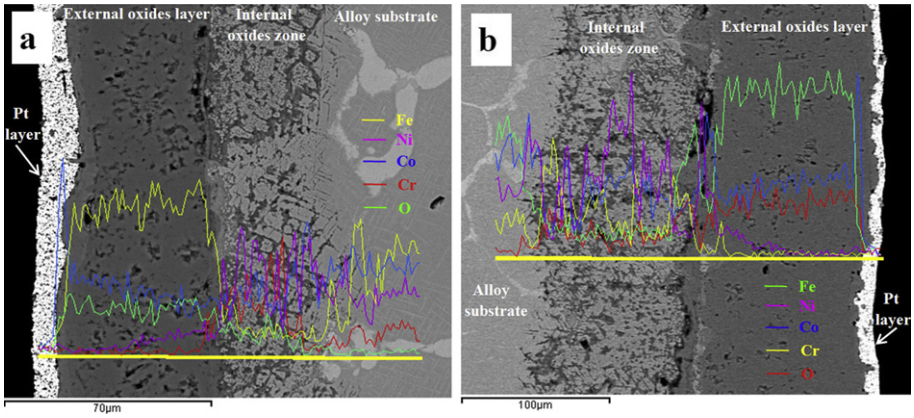

Fig. 9. Cross-sectional morphologies with elements line scan of the cast low-Cr alloy after oxidation in air at 800 °C for 1 week (a) and 6 weeks (b), respectively.

layer. As a result, preferential oxidation of Cr was promoted. Importantly, the sputtered nanocrystalline coating contained a large number of interfaces or grain boundaries (Fig. 2) that could acted as channels for Cr outward diffusion from the coating substrate [25], enhancing transport of Cr to the spinel/coating interface to support the growth of a Cr_2O_3 inner layer, subsequently leading to the formation of the continuous Cr_2O_3 inner layer. Following the formation of the Cr_2O_3 inner layer, Nb was enriched at the coating/Cr_2O_3 interface as a result of the depletion of Fe,Co,Ni and Cr. Moreover, the oxygen partial pressure at that interface was further decreased, resulting in the formation of Nb_2O_5. Then the solid state reaction between Cr_2O_3 and Nb_2O_5 occurred, leading to the formation of $CrNbO_4$. It is obvious that the sputtered surface nanocrystallizaion of the low-Cr alloy has significantly changed the surface scale structure in comparison with the cast low-Cr alloy after oxidation. The continuous Cr_2O_3 inner layer noticeably improved the oxidation resistance, and the low-Cr-containing $(Co,Fe)_3O_4$ spinel outer layer effectively reduced the Cr outward migration.

3.4. Electrical properties of the surface scale

Fig. 12 presents the surface scale ASRs (600–800 °C) of the sputtered low-Cr alloy coating after oxidation in air at 800 °C for 1 week and 12 weeks, respectively. For comparison, the surface scale ASRs of the cast alloy after oxidation for 1 week and 6 weeks were also included. For the cast alloy and the sputtered coating, respectively, as shown in Fig. 12, the scale ASRs increased with the increase in thermal exposure time, i.e. the scale ASR for the cast alloy after 6-week oxidation (cast alloy-8A-6W) was higher than that after 1-week oxidation (cast alloy-8A-1W). Similarly, the ASR of the scale formed on the sputtered coating after 12-week oxidation (sputtered coating-8A-12W) was higher than that after 1-week oxidation (sputtered coating-8A-1W). Obviously, the scale ASR of the sputtered coating was higher than that of the cast alloy. Especially, the scale ASR for the sputtered coating only after 1-week thermal exposure was higher than that for the cast alloy after 6-week oxidation. Furthermore, the scale ASR of the sputtered coating after 12-week oxidation exhibited the highest value among all the tested samples. The higher scale ASR for the sputtered coating should be primarily correlated to the surface scale structure. As demonstrated in Figs.9 and 11, the external oxides layer formed on the cast alloy contained two layers with a thin outer layer of Co_3O_4 and a thick inner spinel layer of $(Co,Fe)_3O_4$. Both of them have a higher electrical conductivity than Cr_2O_3 [26–29]. The internal oxide mainly rich in Cr was discontinuous, thus it could not adversely affect the scale electrical conduction. Nevertheless, as shown in Figs. 10 and 11, the oxide scale formed on the sputtered coating after thermal exposure consisted mainly of $(Co,Fe)_3O_4$ spinel outer layer and a continuous Cr_2O_3 inner layer. Although the oxide scale formed on the sputtered coating was much thinner than that on the cast alloy, the scale ASR for the sputtered coating was higher than that for the cast alloy due to the fact that the Cr_2O_3 has a lower electrical conductivity than Co_3O_4 and $(Co,Fe)_3O_4$. In addition, the contact or interfacial resistance between Pt current collector and Co_3O_4 might be lower than that between Pt layer and

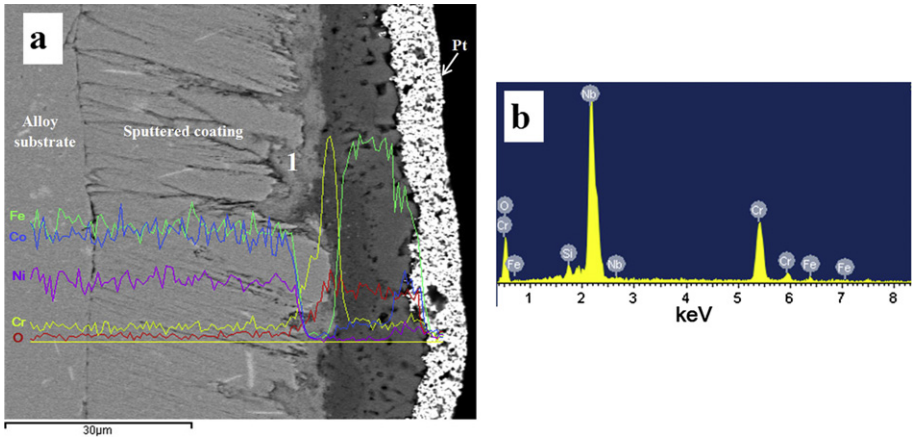

Fig. 10. Cross-sectional morphology with elements line scan (a) of the low-Cr alloy sputtered coating after oxidation for 12 weeks in air at 800 °C, (b) EDX spectra from point 1.

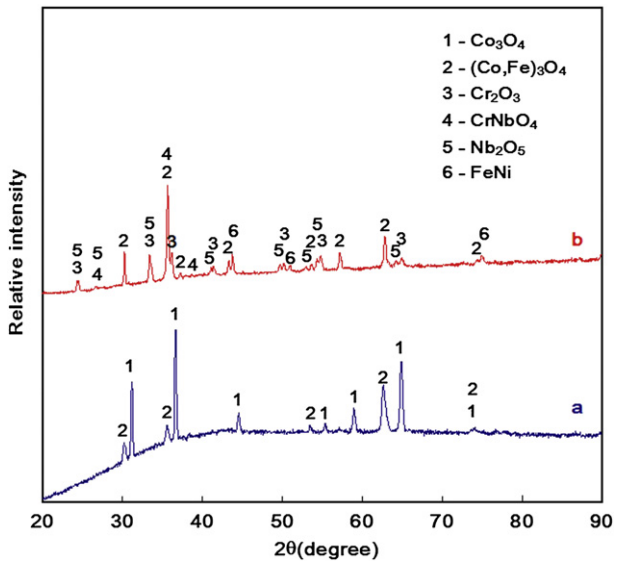

Fig. 11. XRD patterns of the cast alloy and its sputtered coating after thermal exposure in air at 800 °C, (a) the cast low-Cr alloy oxidized for 1 week: (b) the sputtered coating oxidized for 12 weeks.

$(Co,Fe)_3O_4$ spinel layer, which could also contribute to a lower scale ASR for the cast alloy than that for the sputtered coating.

Even though the sputtered coating exhibited a higher scale ASR than the cast alloy, the scale ASR (31.97 mΩ cm^2) at 800 °C for the sputtered coating after 12-week oxidation was still in an acceptable level, since it was slightly higher than the ASR (24.4 mΩ cm^2) of the surface scale formed on AISI 430 stainless steel with Mn/Co spinel coating after thermal exposure in air at 800 °C for 1200 h [30]. It should be noted that ASR reflected both the electrical conductivity and the thickness of the oxide scale. The oxide scale thickness of the sputtered coating was related to its specific mass gain that obeyed a parabolic law, as depicted in Fig. 4. Thus, the scale ASR associated with the thickness might also obey a parabolic law. In accordance with the measured data, the scale ASR at 800 °C was 22.04 mΩ cm^2 and 31.97 mΩ cm^2, respectively, after 1-week and 12-week oxidation. The proposed parabolic relationship between ASR and oxidation time can be approximately expressed by:

$$ASR^2 = 48.76t + 437 \quad (3)$$

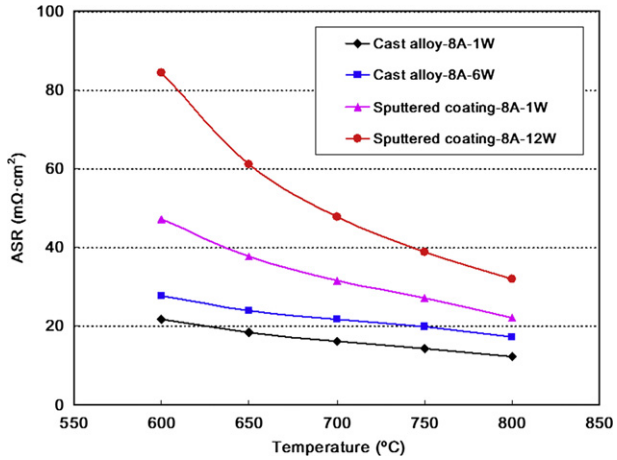

Fig. 12. Scale ASR at temperatures from 600 to 800 °C for the cast alloy and its sputtered coating after oxidation for different time in air at 800 °C.

where ASR is the area specific resistance at oxidation time, *t*. According to Eq. (3), after oxidation for 238.1-week equal to 40,000-h which is the targeted service life of the SOFC at 800 °C, the ASR will be 109.76 mΩ cm^2 slightly higher than 100 mΩ cm^2 which the scale ASR of the SOFC interconnect upon 40,000-h thermal exposure could not exceed. Hence, the sputtered low-Cr alloy coating can almost fulfill the criteria of the scale ASR.

Based on the aforementioned results, a double-layer oxide scale primarily containing an outer layer of $(Co,Fe)_3O_4$ spinel and an inner layer of Cr_2O_3 was successfully formed on the sputtered low-Cr alloy coating after oxidation in air at 800 °C and simultaneously demonstrated a good electrical conductivity. The formation of the continuous Cr_2O_3 inner layer significantly enhanced oxidation resistance of the sputtered low-Cr alloy coating. In spite of containing small amount of Cr in the outer spinel layer as indicated in Fig. 10, the Cr vaporization rate or activity in the spinel phase should be much lower than that in Cr_2O_3 [31]. Thus the low-Cr-containing $(Co,Fe)_3O_4$ spinel outer layer can still act as a barrier to the evaporation of the Cr_2O_3 inner layer. Therefore, the sputtered low-Cr alloy coating exhibited a promising perspective for SOFC interconnects application. However, the Cr content in the sputtered low-Cr alloy coating was lower than that in commercial stainless steels interconnect, so the longer test should be carried out to assess its oxidation resistance with time. Furthermore, as shown in Fig. 10, the Si oxide was still detected below the Cr_2O_3 layer. Although it was not continuous, a further investigation for the sputtered coating of a Si-free low-Cr alloy should be conducted in future to avoid the adverse effect of Si oxide on the scale ASR after long-term operation.

4. Conclusions

From the results above, the following conclusions can be drawn.

(1) The sputtered nanocrystalline coating of the low-Cr Fe–Co–Ni alloy with 0.36wt.% Si significantly improved oxidation resistance in air at 800 °C.
(2) After 12-week oxidation in air at 800 °C, the sputtered low-Cr alloy coating thermally developed a double-layer oxide structure with an outer layer of $(Co,Fe)_3O_4$ spinel containing small amount of Ni and Cr atop a continuous inner layer of Cr_2O_3, followed by some oxides including $CrNbO_4$ and Nb_2O_5 with small amount of Si.
(3) The low-Cr-containing $(Co,Fe)_3O_4$ spinel outer layer effectively suppressed the Cr outward migration.
(4) The ASR of the scale formed on the sputtered low-Cr alloy coating after 12-week oxidation demonstrated a quite acceptable value of 31.97 mΩ cm^2, although it was higher than that of the scale grown on the cast low-Cr alloy after thermal exposure.

Acknowledgments

This work was sponsored by the National Natural Science Foundation of China (NSFC) under Grant No. 50971040 and the National Key Basic Research Program of China (973 Program, No. 2012CB625100).

References

[1] S. de Souza, S.J. Visco, L.C. De Jonghe, Solid State Ionics 98 (1997) 57–61.
[2] S. de Souza, S.J. Visco, L.C. De Jonghe, J. Electrochem. Soc. 144 (1997) L35–L37.
[3] H. Ishihara, H. Matsuda, Y. Takita, J. Am. Chem. Soc. 116 (1994) 3801–3803.
[4] P. Huang, A. Petric, J. Electrochem. Soc. 143 (5) (1996) 1644–1648.
[5] K.Q. Huang, R. Tichy, J.B. Goodenough, J. Am. Ceram. Soc. 81 (1998) 2565–2575.

[6] W.J. Quadakkers, J. Piron-Abellan, V. Shemet, L. Singheiser, Mater. High Temp. 20 (2) (2003) 115–127.
[7] Z. Yang, K.S. Weil, D.M. Paxton, J.W. Stevenson, J. Electrochem. Soc. 150 (9) (2003) A1188–A1201.
[8] J.W. Fergus, Mater. Sci. Eng. A397 (2005) 271–283.
[9] S. Linderoth, P.V. Hendriksen, M. Mogensen, N. Langvad, J. Mater. Sci. 31 (1996) 5077–5082.
[10] S. Geng, J. Zhu, Z.G. Lu, Solid State Ionics 177 (2006) 559–568.
[11] J. Li, J. Pu, B. Hua, G. Xie, J. Power Sources 159 (2006) 641–645.
[12] Z. Yang, P. Singh, J.W. Stevenson, G. Xia, J. Electrochem. Soc. 153 (2006) A1873–A1879.
[13] H. Kurokawa, K. Kawamura, T. Maruyama, Solid State Ionics 168 (2004) 13–21.
[14] J. Pu, J. Li, B. Hua, G. Xie, J. Power Sources 158 (2006) 354–360.
[15] M. Han, S. Peng, Z. Wang, Z. Yang, X. Chen, J. Power Sources 164 (2007) 278–283.
[16] P. Kofstad, R. Bredesen, Solid State Ionics 52 (1992) 69–75.
[17] Y. Matsuzaki, I. Yasuda, Solid State Ionics 132 (2000) 271–278.
[18] S.C. Paulson, V.I. Birss, J. Electrochem. Soc. 151 (2004) A1961–1968.
[19] S. Taniguchi, M. Kadowaki, H. Kawamura, T. Yasuo, Y. Akiyama, Y. Miyaki, T. Saitoh, J. Power Sources 55 (1995) 73–79.
[20] J.Y. Kim, V.L. Sprenkle, N.L. Canfield, K.D. Meinhardt, L.A. Chick, J. Electrochem. Soc. 153 (2006) A880–A886.
[21] S. Geng, J. Zhu, M.P. Brady, H.U. Anderson, X. Zhou, Z. Yang, J. Power Sources 172 (2007) 775–781.
[22] S. Geng, S. Qi, Q. Zhao, Z. Ma, S. Zhu, F. Wang, Mater. Lett. 80 (2012) 33–36.
[23] S. Geng, Y. Li, Z. Ma, L. Wang, L. Li, F. Wang, J. Power Sources 195 (2010) 3256–3260.
[24] S. Geng, F. Wang, S. Zhang, Suf. Coat. Technol. 167 (2003) 212–216.
[25] X. Peng, J. Yan, F. Wang, Act. Mater. 53 (2005) 5079–5088.
[26] W. Zhu, S.C. Deevi, Mater. Sci. Eng. A348 (2003) 227–243.
[27] J. Zhu, S. Geng, D.A. Ballard, Int. J. Hydrogen Energy 32 (2007) 3682–3688.
[28] A. Petric, H. Ling, J. Am. Ceram. Soc. 90 (2007) 1515–1520.
[29] Z. Bi, J. Zhu, J.L. Batey, J. Power Sources 195 (2010) 3605–3611.
[30] J. Wu, C.D. Johnson, Y. Jiang, R.S. Germmen, X. Liu, Electrochimica Acta 54 (2008) 793–800.
[31] K.A. Nielsen, A.R. Dinesen, L. Korcakova, L. Mikkelsen, P.R. Hendriksen, F.W. Poulsen, Fuel Cells 2 (2006) 100–106.